[Link to publication](#)

**University of Bath**

# The structure of low-Froude-number lee waves over an isolated obstacle

**Stuart B. Dalziel[1]†, Michael D. Patterson[2], C. P. Caulfield[3,1] and Stéphane Le Brun[1,4]**

[1] Department of Applied Mathematics and Theoretical Physics, University of Cambridge, Wilberforce Road, Cambridge CB3 0WA, UK

[2] Department of Architecture and Civil Engineering, University of Bath, Bath BA2 7AY, UK

[3] BP Institute, University of Cambridge, Madingley Road, Cambridge CB3 0EZ, UK

[4] École Polytechnique, Route de Saclay, 91120 Palaiseau, France

We present new insight into the classical problem of a uniform flow, linearly stratified in density, past an isolated three-dimensional obstacle. We demonstrate how, for a low-Froude-number obstacle, simple linear theory with a linearized boundary condition is capable of providing excellent quantitative agreement with laboratory measurements of the perturbation to the density field. It has long been known that such a flow may be divided into two regions, an essentially horizontal flow around the base of the obstacle and a wave-generating flow over the top of the obstacle, but until now the experimental diagnostics have not been available to test quantitatively the predicted features. We show that recognition of a small slope that develops across the obstacle in the surface separating these two regions is vital to rationalize experimental measurements with theoretical predictions. Utilizing the principle of stationary phase and causality arguments to modify the relationship between wavenumbers in the lee waves, linearized theory provides a detailed match in both the wave amplitude and structure to our experimental observations. Our results demonstrate that the structure of the lee waves is extremely sensitive to departures from horizontal flow, a detail that is likely to be important for a broad range of geophysical manifestations of these waves.

**Key words:** internal waves, topographic effects

## 1. Introduction

The problem of lee waves in a linearly density stratified flow with steady uniform velocity over topography is an old and well-known problem (e.g. Scorer 1949; Miles 1961; Booker & Bretherton 1967; Turner 1973; Lighthill 1978; Gill 1982; Baines 1995). The wave field that develops is phase-locked with the topography, with the wave crests tilted upstream. In the frame of reference of the topography, the phase velocity has a downward component but is directed parallel to the wave crests, making it appear as though the phase is not propagating. In contrast, the group velocity (and, hence, energy propagation) has an upward and downstream component that is normal

to the wave crests. For a continuous sinusoidal topography $h = \eta_0 \sin k_T x$ of small amplitude $\eta_0$ (with $k_T h_0 \ll 1$), only a single wavenumber $|\mathbf{k}|$ is produced, and even then only provided that $k_T U/N < 1$. Here $k_T$ is the topographic wavenumber, $U$ is the velocity of the mean flow and

$$N = \sqrt{-\frac{g}{\rho_{00}} \frac{\mathrm{d}\rho_0}{\mathrm{d}z}}, \qquad (1.1)$$

is the buoyancy frequency for a Boussinesq stratification $\rho_0(z)$ with reference density $\rho_{00}$ that is acted on by gravity $g$.

When applied to internal gravity waves, the term 'linear' is often used in two different contexts, a situation that can lead to confusion. Here, we use the term 'linear waves' to describe internal gravity waves in which the amplitude of particle displacements $\eta_0$ is small and/or the magnitude of the wavenumber vector $\mathbf{k}$ is small such that $|\mathbf{k}|\eta_0 \ll 1$. For such waves the equations of motion can be linearized, leading to the well-known dispersion relation

$$\frac{\omega}{N} = \cos\theta, \qquad (1.2)$$

where $\omega$ is the angular frequency of the wave in the frame of reference of the fluid and $\theta$ is the angle between the wavenumber vector $\mathbf{k}$ and the horizontal plane (also the angle between the wave crests and the vertical axis). The principle of linear superposition can be applied to such linear waves as there is no dynamical interaction between different wavenumbers or frequencies.

The second use of 'linear' refers to an approach to applying the boundary condition associated with topography. In particular, if the amplitude of the topography $h_0$ is small compared with the length scale of the topography $\lambda_T$, then to the leading order the effect of the boundary on the flow can be linearized such that the boundary condition $w = w_0(x, y)$ is applied at $z = 0$ rather than applying $\mathbf{u} \cdot \nabla(z - h) = 0$ at the surface of the topography $z = h(x, y)$. Here, the linearized boundary condition becomes

$$w_0 = U\frac{\partial h}{\partial x}, \qquad (1.3)$$

in which the linear wave assumption that the velocities induced by the topography are small compared with the mean flow has been applied.

It is worth noting that we have made use of two natural frames of reference in the discussion so far. For most of what follows we use the frame of reference of the topography in which the flow is steady (or quasisteady) with coordinates $\mathbf{x} = (x, y, z)$. There will be times, however, where the (Lagrangian) frame of reference of the fluid is more useful. In this latter frame the flow is oscillatory with coordinates $\mathbf{X} = (X, Y, Z)$. These two coordinate systems are related through $\mathbf{X} = \mathbf{x} + \mathbf{U}t$. The geometric configuration of the wave crests is, of course, identical between the two fames of reference, but the Doppler-shifted wave frequency $\omega_T$ in the topographic frame is zero.

It is widely recognized that for linear waves, the wave field produced by an isolated obstacle may be constructed readily from those generated by sinusoidal topography by the principle of linear superposition, provided the height of the obstacle is small compared with its length. In particular, we need to be able to apply the linearized boundary condition (1.3) for all Fourier components of the topography $\hat{h}(k_T)$, thus requiring $k_T\hat{h} \ll 1$. As before, waves can propagate away from the topography only

provided $k_T U/N < 1$, thus providing a cut-off of the higher topographic wavenumber components. As the Fourier transform $\hat{h}(k_T)$ of an isolated obstacle of length $L$ described by height $h(x)$ will have $\hat{h}(k_T) \neq 0$ for (almost) all $k_T$, there will always exist Fourier components in the range $0 \leqslant k_T < N/U$ for which internal waves are excited, regardless of the streamwise Froude number $F_L = U/LN$. In the frame of reference of the fluid these waves have different angular frequencies given by $\omega = k_T U$ and, hence, $\cos\theta = k_T U/N$ so that the associated waves propagate at different angles.

Implicit in the linearized boundary condition is the assumption that the mean flow can rise up and over the topography. Noting that the work required in a linear stratification to raise a parcel of fluid by height $h_0$ is $\frac{1}{2}gh_0^2 \, d\rho_0/dz$ while the kinetic energy available to do so is $\frac{1}{2}\rho_{00}U^2$ leads naturally to the condition

$$F_h = \frac{U}{Nh_0} \geqslant 1, \tag{1.4}$$

where $F_h$ is the topographic Froude number. Interestingly, it is in the small $F_h$ limit that nonlinearities are most important (Miles 1961; Wurtele, Sharman & Datta 1996), and it is in this limit that there has been the least experimental progress, even in the simplest uniform-flow case.

In this article we tackle the problem where $F_h \ll 1$ and so the flow does not contain sufficient energy to simply rise up and over the topography. For two-dimensional problems, this subcritical limit leads to 'blocking' (Long 1955; Baines 1987) where a stagnant layer forms upstream of the topography, altering the structure of the approaching velocity field. Less is known, however, about the equivalent three-dimensional problem where fluid can move around the obstacle rather than over it.

Drazin (1961) suggested that, for a compact isolated three-dimensional obstacle on an otherwise flat plane, the flow could be divided into two regions. Below some critical height $z_c < h_0$, the flow would be essentially two-dimensional, moving horizontally in a layer-wise fashion around the obstacle. The region of the flow above $z_c$ has sufficient energy for it to be raised up and over the obstacle. Greenslade (1994, 2000) extended the ideas of Drazin (1961) and suggested that, for a hemisphere of radius $R$, only streamlines above

$$z_s = (1 - AF_R)R, \tag{1.5}$$

far from the obstacle pass over the obstacle and make the vertical excursions that lead to internal waves. Here,

$$F_R = \frac{U}{NR}, \tag{1.6}$$

and $A$ is a constant. Streamlines for $z < z_s$ remain essentially horizontal and pass around the obstacle instead. Greenslade (2000) suggested $A \sim O(1)$ and is independent of the Froude number while experimental measurements by Vosper *et al.* (1999) confirmed $A \sim 1$. More recently, Voisin (2007) has provided a detailed theoretical analysis of the wave field under these assumptions. Note that for the hemisphere, $F_R = F_h = 2F_L$. We henceforth refer to $F_R$ as the 'topographic Froude number'. As we shall see, this separation into two regions opens the possibility of using a linearized boundary condition for low $F_R$, avoiding the problems of overturning streamlines discussed by Miles & Huppert (1968) and Huppert & Miles (1969).

Both the two-dimensional and three-dimensional versions of blocking rely on upstream propagation of information to change the structure of the approaching flow

during its initial establishment. Indeed, there is the potential for upstream propagation of information in a channel of depth $D$ whenever the 'channel Froude number'

$$F_D = \frac{U}{ND} < \frac{1}{\pi}.$$  (1.7)

(Long 1955). Since $D$ necessarily exceeds $R$, then $F_D < F_R$. For the work we present here, $F_D$ is comfortably less than $1/\pi$ and upstream propagation is possible. We return to this issue later.

In this paper we explore the behaviour of internal waves generated by a hemisphere at very low topographic Froude number in a stratified channel. In § 2 we describe the experimental set-up before presenting our basic observations in § 3. In § 4 we explore the lee waves in greater detail, discussing their establishment through acceleration of the flow and issues of causality before using a linearized boundary calculation in an attempt to predict the wave field. Analysis of the results of this calculation highlights both agreement and discrepancies with the experimental measurements. A modified linearized theory is presented in § 5, leading to a significant improvement in the level of agreement with the experiments. Finally, our conclusions are presented in § 6.

## 2. Experimental set-up

The experiments described here were performed in a stratified shear flume based on the original design of Odell & Kovasznay (1971). The flume, sketched in figure 11(*a*), is filled with saltwater using the normal double-bucket technique to produce a stable linear density stratification with buoyancy frequency $N$ that was varied from 1.13 to 1.75 rad s$^{-1}$ between the experiments. In all cases the channel was filled to a depth of $H = 300$ mm and the density profile for each experiment was measured by traversing an aspirating conductivity probe, these measurements calibrated by direct samples whose densities were determined using a Paar density meter. Figure 1(*b*) shows a typical density profile. The flow is driven around the race-track-like circuit of the flume through the viscous boundary layers on two stacks of intermeshing discs rotating about vertical axes. In our version of the flume, each stack of 18 concentric discs is divided into 6 groups of 3 discs, with a separate brushless DC servo motor driving each set through a column in the centre of each stack of discs. Shear flows can be developed by driving discs at different heights at different rotation rates, although in this paper we rotate all of the discs at the same speed to obtain a uniform flow.

We may model the barotropic response of the fluid within the flume in a simple manner if we assume both the drive mechanism (acting through viscous stresses on the discs) and the friction the flow experiences around the channel are linear processes. In particular, we propose

$$\frac{\mathrm{d}U}{\mathrm{d}t} = \frac{1}{\tau}(a\Omega - U),$$  (2.1)

where $\Omega = \Omega(t)$ is the rotation rate of the discs, $a$ is a constant length scale combining the geometry of the discs with the relative viscous stresses on the discs and channel walls, and $\tau$ is a constant time scale representing the inertia of the system. In deriving this model we have ignored all wave motions, both within the fluid and on the free surface. For the experiments reported here, the discs were accelerated from rest to $\Omega = \Omega_\infty$ over 2 s, and so we may take $\Omega$ as a step function and solve (2.1) to obtain

$$U = U_\infty(1 - \mathrm{e}^{-t/\tau}),$$  (2.2)
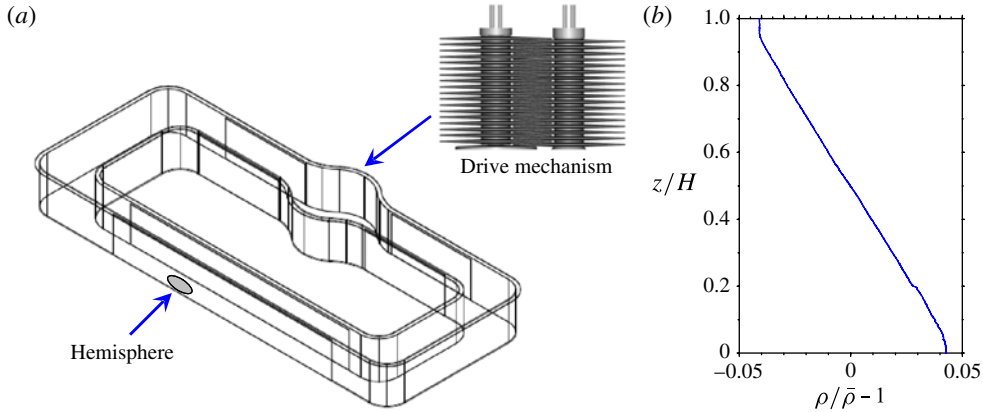
(a)



Hemisphere

Drive mechanism

(b)

FIGURE 1. (Colour online available at journals.cambridge.org/flm) Schematic of the stratified shear flume. (a) Outline of the channel and intermeshing discs of drive mechanism. (b) Typical density stratification.
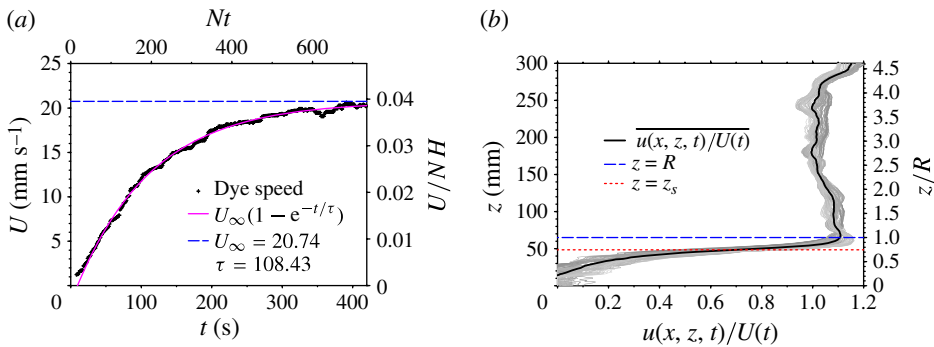


FIGURE 2. (Colour online) Mean flow within the channel. (a) Acceleration of flow in response to the near-impulsive acceleration of the discs. (b) Normalized vertical velocity profile behind the obstacle. The profile, obtained from dye streaks, represents the mean for $t > 200$ s over the region downstream of the obstacle. The range of the individual profiles is indicated in grey.

where $U_\infty$ is the asymptotic flow speed at late time. Figure 2(a) demonstrates the applicability of this model using velocity measurements during the acceleration of the flow. The velocity measurements are obtained from dye streaks resulting from dropping $KMnO_4$ crystals through the depth of the tank. We find the e-folding time scale as $\tau = 110 \pm 15$ s, depending on $U_\infty$, suggesting some weak nonlinearity in the system. Although initially the vertical profile of the velocity is non-uniform, from $t \approx 70$ s the profile is uniform to within $\pm 10\%$ in the absence of the obstacle, except very close to the lower boundary.

The $R = 65$ mm radius hemispherical obstacle was positioned on the floor of the channel in the 2.4 m working section. The diameter of this obstacle should be compared with the $B = 200$ mm width and $H = 300$ mm depth of the working section. It is clear that there will be some acceleration of the base flow due to the 11 % blockage of the available cross-sectional area. In addition, the presence of the sidewalls will play some role. We return to both of these aspects later. The

obstacle also affects the mean velocity profile within the channel. While the velocity profile still collapses and remains uniform to within $10\%$ above the height of the obstacle, it takes on a more complex form in the lower regions. Figure 2(*b*) illustrates the collapse of the accelerating profiles for $t > 70$ s in a region downstream of the obstacle. Horizontal lines show both $z = R$, the top of the obstacle, and $z = z_s$ (under the assumption that $A = 1$), illustrating that there is some difference between the flow around the obstacle for $z < z_s$ and that over the obstacle for larger $z$. We discuss later the mechanisms at work here and their impact on the flow.

Quantitative measurements of the internal wave field employed Synthetic Schlieren (Dalziel, Hughes & Sutherland 1998, 2000; Sutherland *et al.* 1999; Dalziel *et al.* 2007). By placing a strongly illuminated texture pattern on one side of the working section and viewing it through the channel with a digital video camera, small apparent movements of the texture can be related to perturbations in the gradient of the refractive index field and, hence, the density perturbations caused by internal waves generated by the topographic feature. As demonstrated by Scase & Dalziel (2006), if the density perturbations are an even function of position about the central plane of the flume, then the signal recorded by Synthetic Schlieren is proportional to the cross-channel (line-of-sight) mean of the gradient in the density perturbation normal to the viewing axis. Thus, with the arrangement used here, Synthetic Schlieren returns directly the cross-channel average perturbation buoyancy gradients

$$b_x = \overline{b'_x} = -\frac{g}{\rho_{00}}\frac{\partial \overline{\rho'}}{\partial x} \quad \text{and} \quad b_z = \overline{b'_z} = -\frac{g}{\rho_{00}}\frac{\partial \overline{\rho'}}{\partial z}, \tag{2.3}$$

where the overbar represents a cross-channel average and $\rho\prime$ is the wave-induced density perturbation to the background stratification $\rho_0$. Although we are able to integrate this gradient field (see Hazewinkel, Grisouard & Dalziel 2010) to determine the cross-channel averaged buoyancy perturbation $b = \overline{b'} = -(g/\rho_0)\overline{\rho'}$, most of our discussion will concentrate on $b_x$ as linear wave theory relates this to the vertical velocity of the wave field by

$$b'_x = \frac{N^2}{U}w'. \tag{2.4}$$

We report on two sets of experiments. In a preliminary set of steady experiments we employed a Jai CVM4 + CL digital video camera with a resolution of $1320 \times 1024$ pixels, while in a later set exploring the establishment of the flow we employed a Dalsa 4M60 digital video camera with a resolution of $2352 \times 1728$ pixels, recording 10 frames per second. In both cases we utilized 8-bit images. In the first set a region slightly under 900 mm in length was visualized with the camera 5 m from the tank, while in the latter set these values were increased to around 1300 mm and 6.5 m, respectively. The Synthetic Schlieren pattern, located 500 mm behind the tank, comprised randomly positioned clear dots on a black background, printed on overhead projector transparency film and illuminated by a bank of fluorescent tubes. The camera was controlled and all of the analysis undertaken using DigiFlow.

Unfortunately, the rotation of the discs generates some fine-scale disturbances. While these have a negligible impact on the internal waves, their presence in the field of view disrupts the imaging of the pattern and reduces the quality of the Synthetic Schlieren results. For this reason, we restrict our attention to the period $t < L_C/U_\infty + \tau(1 + W_p(\exp(-1 - L_C/U_\infty\tau)))$, where $L_C$ is the distance between the discs and the obstacle and $W_p(\cdot)$ is the 'Lambert $W$ function' or 'product log' (the principal solution $w(v)$ is the inverse of $v = we^w$). In practice, we limit our observations to
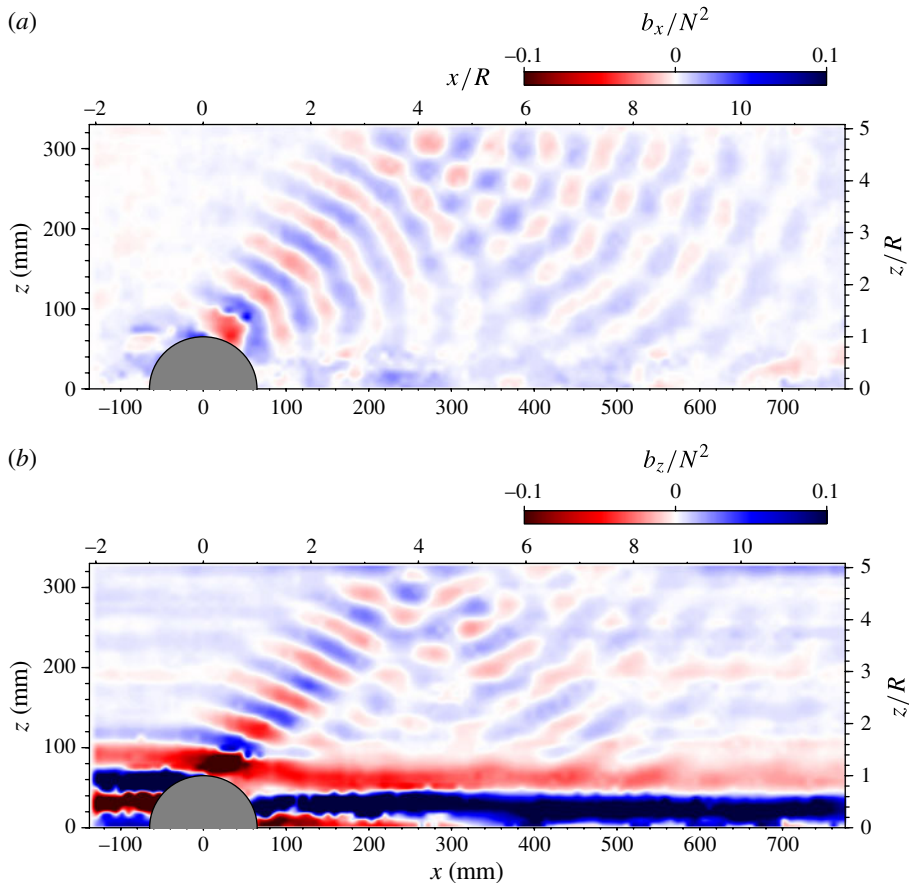
(*a*)



(*b*)



FIGURE 3. Observed $b_x$ (*a*) and $b_z$ (*b*) perturbation buoyancy gradient fields for the $F_R = 0.13$ experiment. Here, the obstacle is mounted on the base of the tank and the flow is nominally uniform from left to right.

the initial 350 to 750 s, depending on the selected $U_\infty$, to avoid contaminating the results. Since this period is between $3\tau$ and $8\tau$, the mean velocity at the end of the observational period is always close to the asymptotic value $U_\infty$, and we define our topographic Froude number using this velocity, i.e.

$$F_R = \frac{U_\infty}{NR}. \qquad (2.5)$$

We explore the impact of the initial acceleration of the flow further in § 4.1.

## 3. Basic observations

We consider first an experiment with $N = 1.75$ rad s$^{-1}$ and $U_\infty = 14.8$ mm s$^{-1}$ giving $F_R = 0.13$ and consider the internal wave field at $t = 388$ s, shortly before the fluid initially located by the discs reaches our observation window. By this time the uniform flow velocity is within a few per cent of its asymptotic value. The $b_x$ and $b_z$ fields (figure 3*a*,*b*, determined by the Synthetic Schlieren) give clear evidence of an internal wave field propagating upwards, away from the obstacle, as the waves are swept down stream. These waves are reflected from the free surface and then

propagate back towards the base of the tank as they continue to be carried downstream. The region where the upward and downward propagating waves overlap shows a checkerboard-like pattern due to constructive and destructive interference. Interpreting these images as two-dimensional waves (recall that they are, in fact, the cross-channel mean fields), suggests that the wavelength, and hence $|\boldsymbol{k}|$, is approximately constant, with the strongest waves having $\boldsymbol{k}$ oriented at about $\theta = 45°$ above the horizontal, but with waves existing for most values of $\theta$ in the range $(0, 90°)$. The signal at the lower end of this range, with the wave crests close to vertical, is visible primarily in $b_x$ as the essentially vertical motions have little effect on $\partial \rho\prime / \partial z$. At the $\theta = 90°$ limit, the wave crests and the corresponding motion are essentially horizontal, and the $b_z$ field provides some evidence of such horizontally propagating disturbances confined to the region close to the base of the tank.

In order to simplify our discussion, it is convenient to separate the waves into one of three categories: upward propagating, downward propagating and essentially horizontally propagating. We can achieve this through a simple filtering, similar to the Hilbert transform utilized by Mercier, Garnier & Dauxois (2008) for periodic waves. Here the flow is steady, and so the orientation of the wavenumber vector contains all the relevant information. We begin by performing a two-dimensional fast Fourier transform (FFT) of the $b_x$ and $b_z$ fields (separately), zero padding to compensate for the lack of periodicity in the gradient fields. Using the orientation $\xi = \tan^{-1}(m/k)$ of the corresponding wavenumber vector (in our two-dimensional projection) for each Fourier component, we determine whether the wave is upward propagating $(0 < \xi < 90° - \varepsilon)$ or downward propagating $(0 > \xi > -(90° - \varepsilon))$. We have introduced the constant $\varepsilon$ to allow us to filter out waves that are propagating essentially horizontally. Further, we also filter out from the sets of upward and downward propagating waves the lowest wavenumbers, corresponding to wavelengths greater than or equal to the height of the domain. Finally, we define a third set of waves, comprising all Fourier modes not in either of the first two sets. As we shall see, this set contains the waves that are propagating in an essentially horizontal direction. Figure 4 plots part of the two-dimensional power spectrum for the $b_x$ and $b_z$ fields shown in figure 3 to illustrate the partitioning of the signal into different wave types. Here, following inspection of the spectrum for $b_z$ in figure 4(*e*), we have selected $\varepsilon = 10°$ as this provides a good discriminator of the waves that propagate in an essentially horizontal direction (wavenumber vector close to vertical).

Taking each of these three sets, we can reconstruct the corresponding wave fields in physical space by simply computing the inverse Fourier transforms. Owing to the linearity of this process, and our choice of set definitions, we can recover the full wave field in physical space through simple summation across the three sets of waves.

Utilizing this separation, figure 5 plots the gradient fields for the three sets of waves extracted from the observations shown in figure 3. The upward propagation of the lee waves from the obstacle can be seen clearly in figures 5(*a*) and 5(*b*). These waves form a gradually expanding beam. If the waves had originated at a point source, the beam width would increase approximately linearly away from the obstacle, but here we are still in the near field for this finite obstacle and so the expansion is less evident. This beam is itself comprised of two distinct bands. The wave crests in the larger, stronger upstream band, the 'primary band', are almost straight, with a phase reversal in the weaker, narrower downstream band (the 'secondary band'). This structure is seen most clearly in the $b_z$ field, but is also visible in $b_x$. There is also a hint of additional bands of waves further behind the obstacle. The dominant parts of each wave crest appear to lie along a line at an angle of approximately $45°$ to
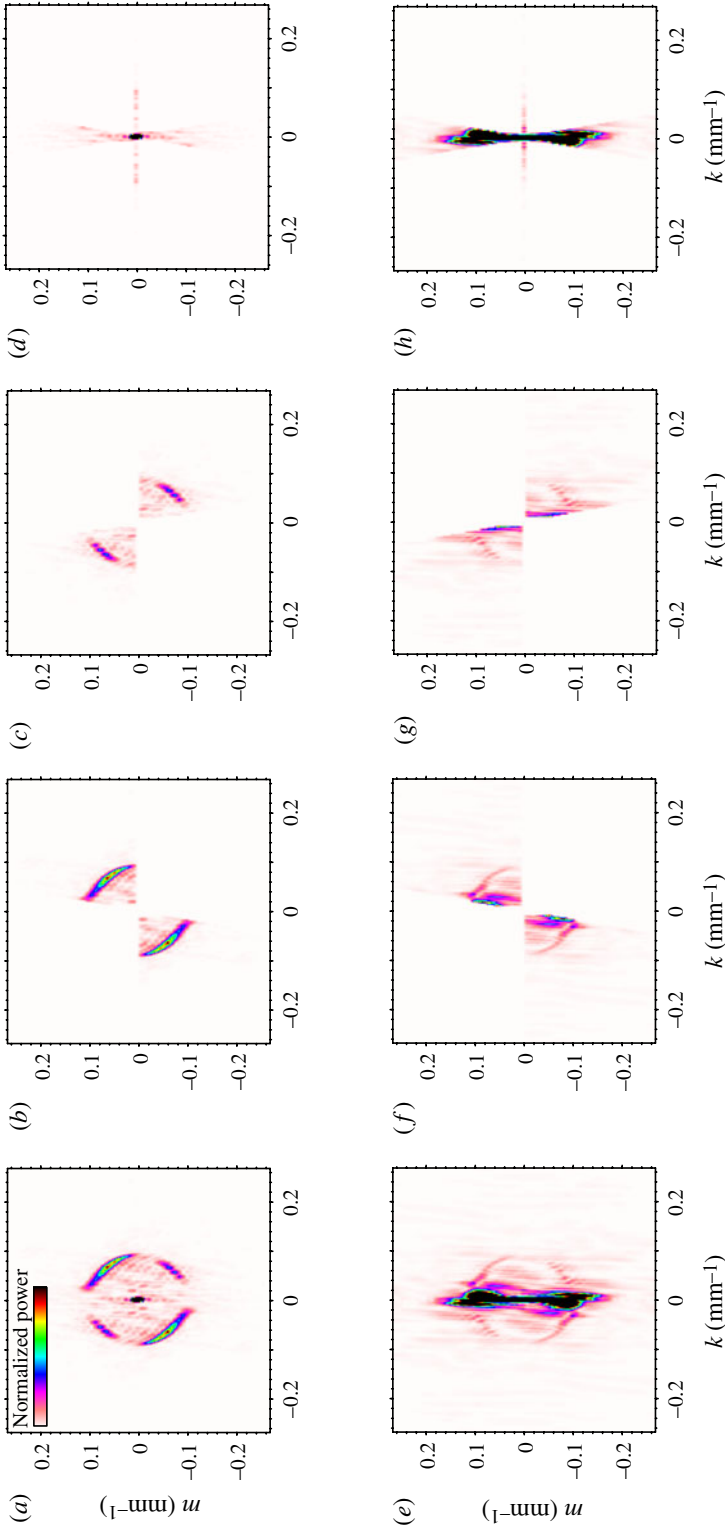
FIGURE 4. Central part of power spectra illustrating the method of separating of waves into their different Fourier components. Spectra for $b_x$ are shown in the top row ($a$–$d$), and $b_z$ are shown in the bottom row ($e$–$h$). The complete spectra are shown in ($a$) and ($e$), with upward-propagating modes shown in ($b$) and ($f$). Downward-propagating modes are shown in ($c$) and ($g$), while the remainder, essentially horizontally propagating modes are in ($d$) and ($h$). The spectra are normalized so that the full extent of the colour bar shown in ($a$) is utilized by the $b_x$ spectrum (the $b_z$ spectra are oversaturated).
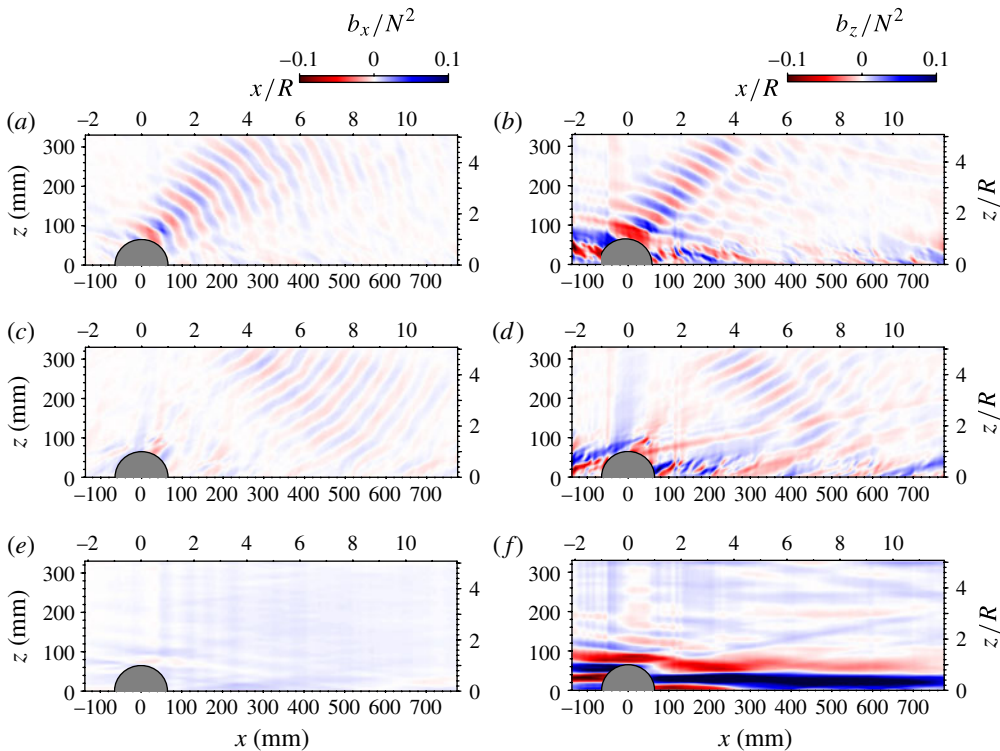
FIGURE 5. The gradient fields for the $F_R = 0.13$ experiment decomposed into (*a,b*) upward-propagating waves, (*c,d*) downward-propagating waves and (*e,f*) essentially horizontally propagating waves. The left-hand column (*a,c,e*) shows $b_x$, while the right-hand column (*b,d,e*) shows $b_z$.
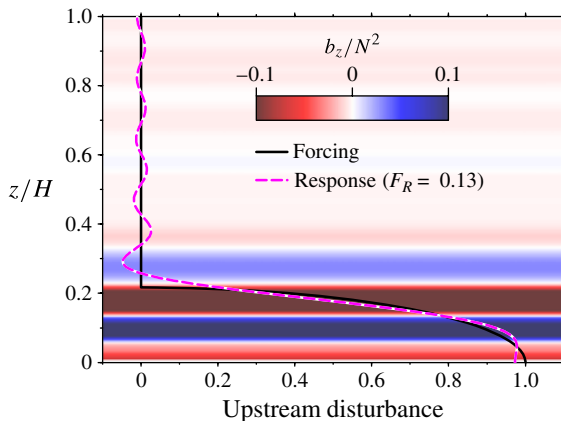


FIGURE 6. Columnar wave modes propagating upstream of the obstacle. The relative forcing (solid line) and response filtered by the propagation condition (dashed line) are shown superimposed on the upstream $b_z$ field.

the horizontal. Outside this beam there is clear evidence of waves with $\boldsymbol{k}$ directed in a more horizontal direction. These waves, which have a higher frequency relative
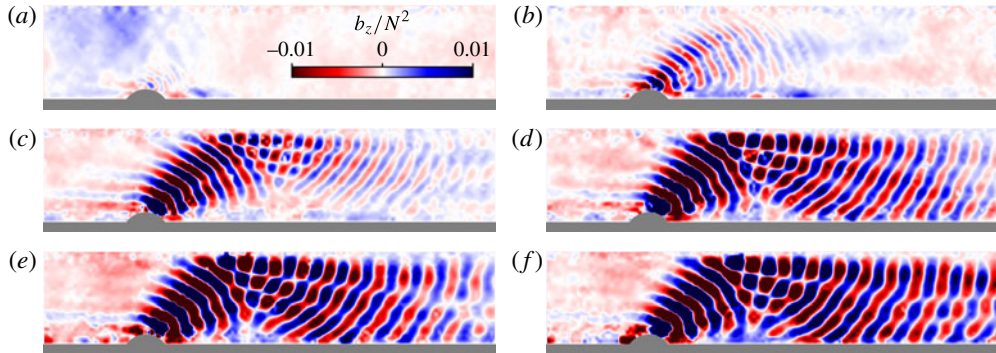
FIGURE 7. (Colour online) Horizontal buoyancy gradient $b_x$ fields during the establishment of the internal wave field for $F_R = 0.18$. The images are saturated at $b_x/N^2 = \pm 0.01$. (a) $t = 70$ s, (b) $t = 120$ s, (c) $t = 170$ s, (d) $t = 220$ s, (e) $t = 270$ s and (f) $t = 320$ s. The colour scale used here (shown in a) is a factor of 10 more sensitive than that used in other figures.

to a frame propagating with the local mean fluid velocity $U_\infty$, have a smaller group velocity and consequently take longer to rise above the obstacle, becoming visible in the $b_x$ field below and to the right of the main beam. Owing to their orientation, the contribution of these waves to $b_z$ is weak, allowing us to see that there are also upward-propagating modes, with a similar wavenumber to that found in the main beam, downstream of the beam. We return to the origin of these waves and the other disturbances seen in the $b_z$ field near the bottom of the channel later.

The upward-propagating waves are the normal lee waves produced by the vertical excursion of fluid over the obstacle, while the downward-propagating waves (figures 5c and 5d) are their reflections from the free surface. In contrast, the essentially horizontally propagating waves (figures 5e and 5f) are dominated by the columnar modes (Long 1955) forced by the finite size of the obstacle causing an upstream blockage and giving rise to the essentially horizontal flow below $z = z_s$.

The simplest model for the blockage by the obstacle is to assume a force distribution proportional to the width of the obstacle, this giving a distribution that decreases as $(1 - z^2/R^2)^{1/2}$ over $0 \leqslant z \leqslant R$. Columnar wave modes exist as a discrete set and the condition for upstream propagation of a particular columnar wave mode $n$ is that $n\pi F_H < 1$ (Long 1955). This means that in the present experiments only the first 11 modes are able to propagate. By taking the Fourier transform of the forcing and retaining only the propagating modes, figure 6 shows how this filtering affects the structure of the upstream disturbance and how the difference between the forcing (solid line) and filtered response (dashed line) is picked out by the observed $b_z$ buoyancy gradient field (background image). Further confirmation of this blocking is provided by the downstream velocity measurements shown in figure 2(b).

## 4. Lee waves

### 4.1. *Establishment*

We begin our more detailed discussion of the lee waves by considering how the wave field becomes established. Figure 7 shows a sequence of $b_x$ fields for an experiment with $U_\infty = 20.7$ mm s$^{-1}$ and $N = 1.74$ rad s$^{-1}$ giving $F_R = 0.18$. In this experiment the discs were accelerated to their steady rotation rate within 1 s, while the e-folding time scale for the flow was around 100 s.

The first response visible in the test section occurs at around 6 s after the discs are initiated. This very weak and nearly symmetric response (barely visible in the neighbourhood of the top of the obstacle) is thought to be due to linear surface modes excited by the acceleration of the discs. Our estimates of the submillimetre free surface displacement give a wavelength of around 530 mm and so a surface wave group velocity of around 0.46 m s$^{-1}$. The time for this first response is therefore consistent with the time for surface waves to traverse the 3 m from the discs to the test section; the 530 mm wavelength is comparable with twice the width of the turning region of the race-track shaped channel, providing a low-wavenumber cut-off for the surface disturbances.

The oscillatory disturbance excited by surface waves soon decays, while a quasisteady (essentially horizontal) disturbance visible in the $b_z$ field at the top of the obstacle gradually increases as the mean flow accelerates. The first lee waves start to become visible at around $t = 50$ s, although the structure is difficult to distinguish until $t \approx 70$ s (figure 7a), where the characteristic pattern of bands of positive and negative $b_x$ first become visible. The flow continues to accelerate as these first lee waves propagate upwards and downstream of the obstacle, so that by $t = 120$ s the wavelength has increased from around 27 to 47 mm. The first waves reach the top of the channel at $t \approx 130$ s, with reflections being well established by $t = 170$ s (figure 7c) when the first reflected waves reach the bottom of the channel. Note that in order to highlight the development at an early stage, the colour scale used for the sequence of images in figure 7 is a factor of 10 more sensitive than that used in the previous section. Unfortunately, this increased sensitivity also highlights the thermal fluctuations in the laboratory and other imperfections.

The amplitude and wavelength continue to increase with the mean flow (figure 7d–f), although the differences decrease with time. This growth can be seen clearly in figure 8 which records the scaled streamwise gradient $b_x/N^2$ field along a line at 45° emanating from the top of the obstacle. Superimposed on the time series is a prediction of the location of the wave crests derived from the linear lee wave theory prediction that $\lambda = 2\pi U/N$ in conjunction with the spin-up model for the shear flume outlined in §2. The virtual time origin here is set at $t = t_0 = 20$ s, comparable with the time required for mode 1 waves to propagate from the rotating discs to the test section of the channel.

Figure 9 shows the evolution of the normalized power spectra for the internal waves for the same times as the $b_x$ fields in figure 7. Again, the expected decrease in wavenumber (increase in wavelength) as the flow accelerates is clearly visible. At early times (figure 9a,b) the only upward-propagating waves are present, revealed by a lack of energy in the second and fourth quadrants. After the waves reflect from the upper boundary, the energy in the second and fourth quadrants increases, although remains small compared with that in the first and third quadrants. Superimposed on these spectra are circles with $|\mathbf{k}|^2 = N^2/U^2$ (with $U(t)$ given by the spin-up model (2.2)), the wavenumber magnitude predicted by two-dimensional linear lee wave theory. (The distribution of power on this locus depends on details such as the shape of the obstacle and the viscous dissipation of the waves.) While there is good general agreement with our observations, it is clear that the magnitude observed for the wavenumber vectors exceeds the expected value when the vector is close to vertical. The equivalent relationship in three dimensions, $|\mathbf{k}|^2 = N^2(k^2 + l^2)/k^2U^2$ can be written as

$$k^2 + m^2 = \frac{N^2}{U^2} + \left( \frac{N^2}{k^2U^2} - 1 \right) l^2, \tag{4.1}$$
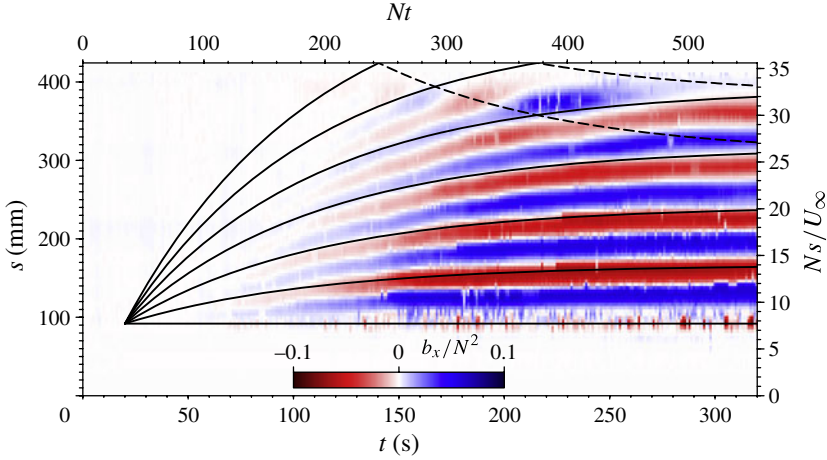
FIGURE 8. Time series of the $b_x/N^2$ field for $F_R = 0.18$ along a section oriented at 45° and passing through the highest point of the obstacle. The superimposed curves are predictions for the location of the wave crests, with dashed lines represented waves reflected from the free surface. The $b_x/N^2$ field is saturated at 0.1 (10 times less sensitive than used for figure 7).
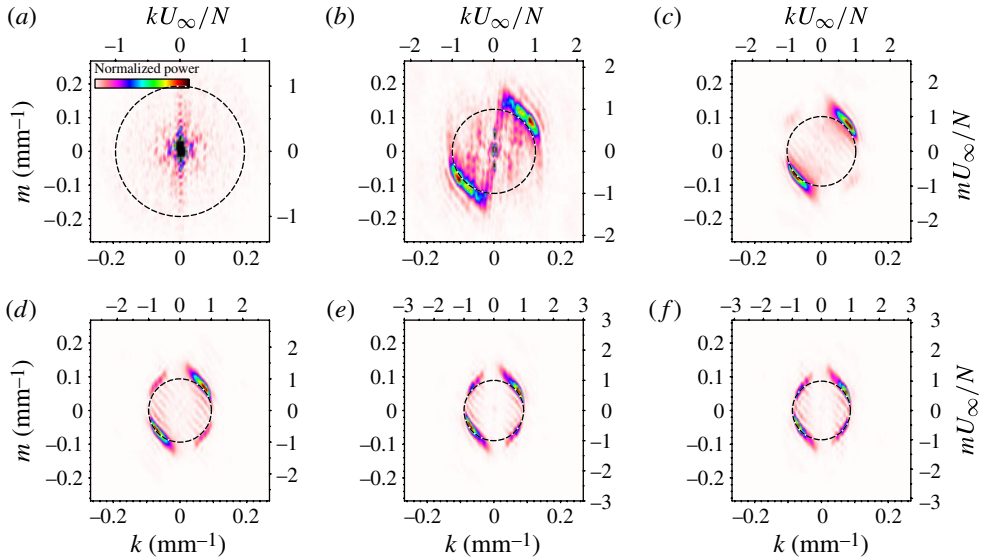


FIGURE 9. Evolution of the normalized power spectrum of the $b_x$ field for $F_R = 0.18$ at (a) $t = 70$ s, (b) $t = 120$ s, (c) $t = 170$ s, (d) $t = 220$ s, (e) $t = 270$ s and (f) $t = 320$ s. The superimposed circles show $|k| = N/U(t)$. The spectra are normalized so that the full extent of the colour bar shown in (a) is utilized at each time.

showing that the presence of the transverse wavenumber $l$ causes an increase in the two-dimensional $(k, m)$ magnitude of the wavenumber that is visible to Synthetic Schlieren since the term in brackets on the right-hand side is necessarily positive for propagating waves. Moreover, this increase is greatest when $k$ is smallest, potentially explaining the angular dependence of the departure from a circle of the spectra in

figure 9. However, as we shall see in §5, there is a more important mechanism that accounts for the non-circular distribution of energy in these spectra.

### 4.2. Causality

In order to compare the lee waves described in the previous section with linear theory, we must understand how the evolution during the establishment of the flow we have seen in the previous section affects the structure of the wave field. For simplicity, we consider a two-dimensional wave field generated by a point source moving horizontally at speed $U(t)$ through an inviscid fluid. The 'principle of stationary phase' (e.g. Lighthill 1978; Voisin 1994) provides the framework for our discussion. While application of this approach to internal waves is not new, we outline the process here as a stepping stone to understanding the wave field.

   This principle of stationary phase is essentially a statement that in the frame of reference of the disturbance, the phase velocity must be parallel with the wave crests (i.e. perpendicular to the wavenumber vector) so that the crests appear to be stationary. Put another way, to an observer in that frame there must appear to be no changes in the structure or phase of the wave field. By defining the phase at some point $x$ as $\phi = k \cdot x - \omega t$, the condition that the phase and structure of the wave field is stationary collapses to differential quantities $\mathrm{d}\phi$, $\mathrm{d}k$ and $\mathrm{d}\omega$ all being zero and that for an observer moving at velocity $U$ relative to the flow,

$$\frac{\partial \phi}{\partial t} + (U \cdot \nabla)\phi = 0. \tag{4.2}$$

Thus, for the phase to be constant relative to the obstacle moving horizontally at speed $U$ relative to the fluid, we have

$$\frac{\partial \phi}{\partial t} + U\frac{\partial \phi}{\partial x} = -\omega + kU = 0. \tag{4.3}$$

Replacing $\omega$ using the dispersion relation and $k = |k|\cos\theta\cos\varphi$ then gives $N/|k| = U\cos\varphi$, where $\varphi$ is the azimuthal angle between the $x$ axis and the horizontal projection of the wavenumber vector. The magnitudes of the phase and group velocities (relative to the fluid) are then

$$|c_p| = U\cos\theta\cos\varphi, \quad |c_g| = U\sin\theta\cos\varphi. \tag{4.4}$$

   For simplicity, consider a steady two-dimensional source of disturbance moving horizontally to the left with constant speed $U$ relative to the frame in which the fluid is at rest. Suppose that a wave propagating at an angle $\theta$ to the vertical is emitted by the source at some location $x_s$ at time $t_s$. At time $t$, an observer moving with the source is now located at $X = x_s - U(t - t_s)$ and the energy in the wave has propagated a distance $r = |c_g|(t - t_s) = U\sin\theta\cos\varphi(t - t_s)$ at an angle $\theta$ to the vertical, so that the energy all lies on a semicircle (in two dimensions) or hemisphere (in three dimensions) spanning between the $x_s$ where the wave was released and the current position $X$ of the disturbance. By considering all previous times for steady $U$ it is easy to show that the internal wave energy is bounded by a 'causality envelope' that propagates as a vertical front colocated with the position of the source. Moreover, lines of constant phase can be readily shown to lie on quarter circles centred on the current location of the source for a two-dimensional disturbance, or spherical surfaces for a three-dimensional disturbance.

   This picture is incomplete if the disturbance has only been travelling for a finite time, as the principle of stationary phase only describes the 'permanent waves' due to
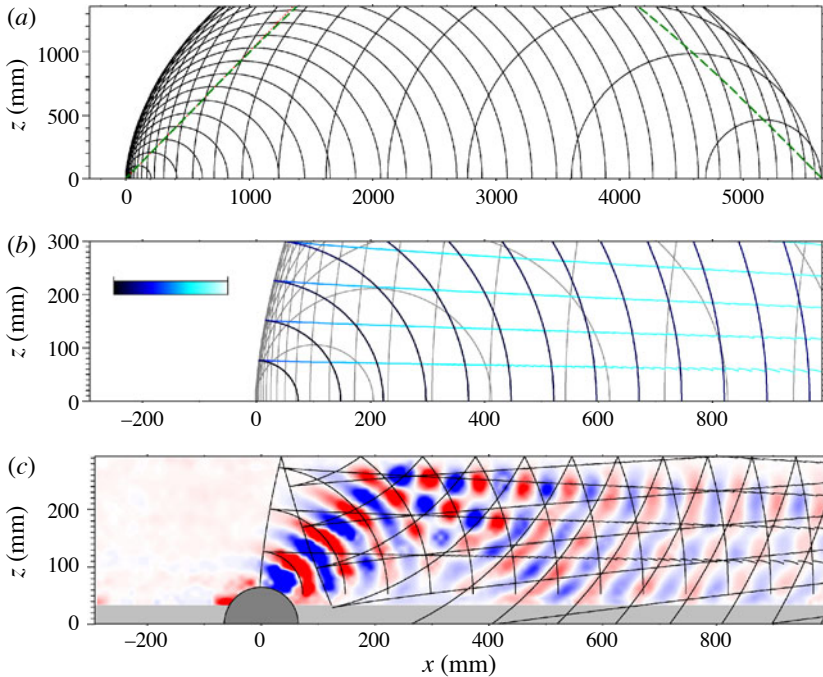
FIGURE 10. (Colour online) Causality of point source in accelerating channel flow assuming no upper boundary. (*a*) Causality shells, drawn at 10 s intervals, for entire evolution. The bold dashed line indicates how a wave released at 45° (dotted line) is swept downstream by the accelerating flow. (*b*) Causality shells (thin grey lines) and phase surfaces (thick lines). The time since the wave was emitted by the source is indicated by the shading of the phase surface. (*c*) Causality envelope and centreline surfaces of constant phase for a point source superimposed on wave field produced by hemisphere for $F_R = 0.13$ at $t = 320$ s.

the steady propagation and not the 'transient waves' due to the impulsive start. It has been shown (e.g. Voisin 1994) that these transient waves match on seamlessly with the permanent waves at the boundary of the causality surface. However, as we shall see shortly, the transient waves are of little importance in the present set-up.

For our present experiment the velocity within the channel relative to the obstacle, $U(t)$, varies continuously with time. While there will be transient waves generated by the gradual acceleration of the flow, the separation between this time scale, $\tau \approx 110$ s, and the typical time scale of the lee waves, $L/U \approx 6$ s, allows us to consider the flow as quasisteady and neglect the transient waves whilst still taking into account important aspects of the establishment of the flow due to the gradual acceleration of the flow in the flume.

Using (2.2) to describe the acceleration of the channel, we can readily construct causality shells and surfaces of constant phase for a point source in the channel. For clarity, figure 10 plots only the situation on the central plane. In particular, figure 10(*a*) shows the semicircular causality shells drawn at 10 s intervals for $0 \leqslant t \leqslant 320$ s, corresponding to the experiment in figure 7. Here we have assumed a fluid of infinite depth although have only plotted the lower portion of this. The overall causality envelope departs from the simple semicircular form of steady propagation due to the acceleration of the flow: waves released at early times are of small wavelength

and propagate only slowly relative to the fluid; these are left increasingly behind the obstacle as the flow accelerates. Even at later times the flow is still not quite at its asymptotic speed and although the causality shells are converging, they do not all lie on top of one another at the source but cross each other. This contrasts with the case of the steady propagation where the shells are all nested within each other.

Figure 10(*b*) provides a zoomed view comparable with the experiment shown in figure 7, but still without reflections from the upper boundary. The causality shells are shown as (parts of) thin grey semicircles. Phase surfaces are also shown as thick lines, drawn at intervals of one wavelength, with their shading indicating the time over which they have been propagating since being released by the moving source. The most recently emitted part of the phase surface is the approximately vertical section near the base of the channel. The waves at this point have a group velocity relative to the fluid tending towards zero and so are simply swept downstream by the mean flow. Moving up and to the left around a particular phase surface, which forms approximately a quarter-circle towards the causality front, the waves get progressively older. We note that the acceleration means the shape of this surface is not actually part of a circle. At the front of the causality envelope the quarter-circle part of the phase surface meets an almost horizontal branch to the phase surface that is due to slower moving waves released at earlier times. The age of the waves increases rapidly as we continue to follow the phase surface along this nearly horizontal branch. The presence of two distinct phase surfaces for each point to the right of the causality envelope gives rise to interference between waves of different $|\boldsymbol{k}|$: a large $|\boldsymbol{k}|$ wave (smaller wavelength) released at an earlier time and a small $|\boldsymbol{k}|$ wave (larger wavelength) released later. This change in wavelength is evident from the convergence of the phase surfaces towards the right-hand side of the figure. The presence of an interference pattern in this accelerating flow contrasts with the case of steady propagation where there is only one phase surface passing through any point within the causality envelope.

Figure 10(*c*) compares the point-source centreline phase surfaces with the experimental observations of $b_x$. Here we have placed the point source at $z = z_s$ on the axis of the hemisphere and we have included reflection from the free surface. Although differences are apparent, there is general agreement in the overall shape of the wave field. The experimental wave field is clearly dominated by the younger waves on the lower branch of the phase surfaces. This is not surprising as the amplitude of the younger waves will be greater initially due to the faster propagation speed, the younger waves have had less time to decay and the younger waves have a longer wavelength and so are less affected by viscosity. If we assume the older branch of the constant phase surfaces does not contribute to the observed wave field (a reasonable assumption given that the observed field decays rapidly towards the causality front), then we can see differences in the shape between the phase surfaces generated by the obstacle and those predicted by the point source. There are two contributing factors here: the obstacle clearly is not a point source; and we are observing the cross-tank mean density gradient field, not simply the centreline structure. We address both of these issues in the next section.

### 4.3. *Linearized boundary*

We have seen so far that we can explain key features of the internal wave field through the principle of stationary phase for an isolated source in a quasisteady flow, although a detailed comparison of the wave field is clearly influenced by the size and shape of the actual source. In this section we explore how we can model this low topographic

Froude number flow using a linearization of the boundary despite the hemispherical nature of the obstacle ensuring its horizontal and vertical scales are comparable. We start by employing the Drazin–Greenslade separation of the flow into two regions: an essentially horizontal flow near the base of the obstacle and a wave-generating flow near the top of the obstacle. For the present purposes, we simplify the original approach and just choose $A = 1$ in (1.5) (this choice being compatible with the results of Vosper *et al.* 1999) and assume that there is a horizontal stream surface at height

$$z_s = (1 - F_R)R \qquad (4.5)$$

everywhere along the channel and ignore the flow below this height. As we shall see later, the choice of $A = 1$ provides good quantitative agreement for the energy in the wave field. We therefore consider a domain in which the obstacle is reduced to a hemispherical cap of height $F_R R$ and length (and width) $2R\sqrt{F_R(2 - F_R)}$. For small $F_R$ the aspect ratio of the cap therefore scales as $2^{3/2}F_R^{1/2}$ and so is small, allowing us to linearize the cap (at least for the lower wavenumber components) and impose the boundary condition in terms of $w = U\partial h/\partial x$ at $z = z_s$.

To simplify the calculation, we assume a steady flow in a periodic channel with length 32 times the width and utilize FFTs on a grid of the channel with $4096 \times 128$ mesh points in a horizontal plane such that the forcing in Fourier space is

$$\hat{W}(k, l) = kU\hat{h}(k, l), \qquad (4.6)$$

where the three-dimensional wavenumber vector $\boldsymbol{k} = (k, l, m)$. Noting that phase locking the waves restricts us to negative $k$ with real $m$ given by

$$m = -\left(N^2/(k^2 U^2) - 1\right)^{1/2}\left(k^2 + l^2\right)^{1/2}, \qquad (4.7)$$

then in three-dimensional Fourier space the horizontal buoyancy gradient is given by

$$\hat{b}'_x(k, l, z) = \begin{cases} N^2 k\hat{h}(k, l)e^{imz}, & -\dfrac{N}{U} < k < 0, \\ 0, & \text{otherwise.} \end{cases} \qquad (4.8)$$

Transforming $\hat{b}'_x(k, l, m)$ back to real space gives $b'_x$ throughout the three-dimensional volume and by computing the cross-tank average we recover our first estimate for the two-dimensional $b_x$ shown in figure 11(*a*).

Although there are clear similarities between figure 11(*a*) and the corresponding experimental results of the upward-propagating waves shown in figure 5(*a*) (repeated in the inset image), there are also clear differences. First, as discussed above, the experiments have only had a finite time to develop so that causality restricts the domain in which wave motions can occur. Second, molecular viscosity causes the waves to decay with time (and, hence, distance) from the source. It is possible to include these effects in a number of ways.

The first step of the very simple approach we use here is to employ the three-dimensional causality from a point source modelling the transient acceleration of the flow to compute where waves may be found, and simply discard any permanent waves seen in figure 11(*a*) that fall outside this region. While this approach is valid for a point source, here we are considering the near field of a finite size obstacle and so there will be some details not captured by this approach. We return to this issue in § 6.

Two options exist for determining the viscous attenuation. Here we have used the vertical component of the group velocity to determine propagation time and thus
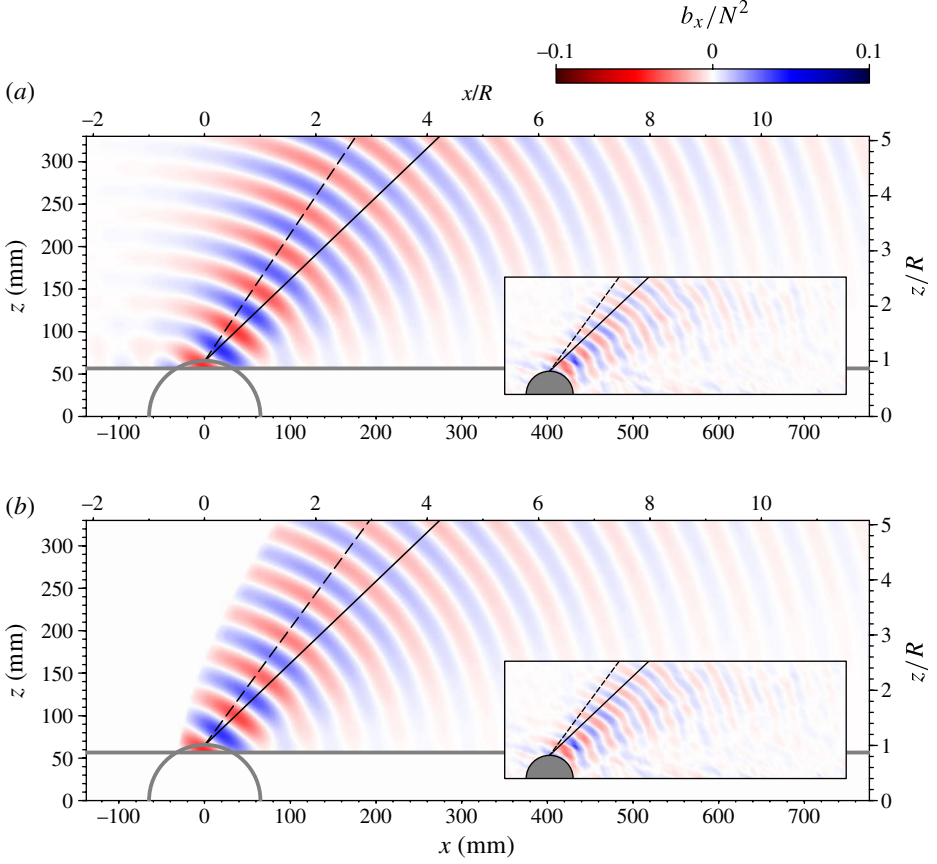
FIGURE 11. Buoyancy gradient field $b_x/N^2$ obtained using the linearized boundary approximation. (*a*) Inviscid calculation with no causality imposed and (*b*) viscous calculation using causality based on a point source. For both, the inset image (seen previously in figure 5*a*) shows the corresponding experimental image and the rays from the top of the obstacle are shown at angles of $\Theta_{300} = 44.0°$ (solid line) and $\Theta_{lin} = 56.3°$ (dashed line) to the horizontal; see § 4.5 for details.

replaced (4.8) with

$$\tilde{b}'_x(k, l, z) = \begin{cases} N^2 k \hat{h}(k, l) \mathrm{e}^{(im - \beta)z}, & -\dfrac{N}{U} < k < 0, \\ 0, & \text{otherwise}, \end{cases} \quad (4.9)$$

where

$$\beta = \frac{\nu}{2N} \frac{|\boldsymbol{k}|^5}{|m| (k^2 + l^2)^{1/2}} \quad (4.10)$$

for a high-Schmidt-number fluid (in which the diffusivity of density is negligible compared with viscosity). The result of this calculation is shown in figure 11(*b*). The impact of causality is obvious, with the well-defined curved leading edge of the wave field. The viscous attenuation is also clear, both through weaker waves downstream at small heights, and with the tapering off of $b_x$ towards the causality envelope. With all
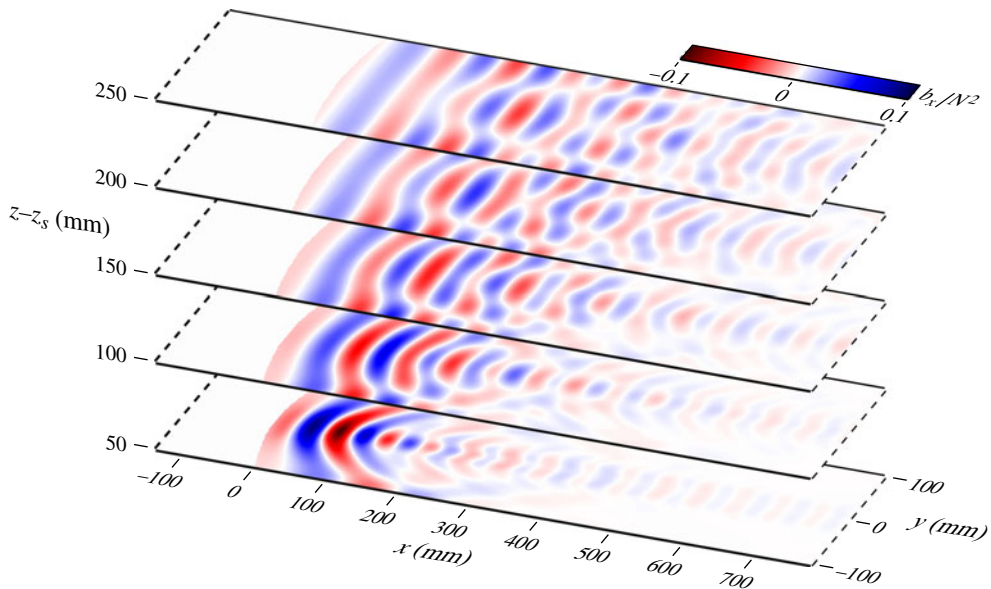
FIGURE 12. Cross-channel structure of $b'_x$ from linearized boundary calculation at 50 mm intervals above $z_s$ for a spherical cap.

waves having the same $|\boldsymbol{k}|$, the impact of viscous attenuation is primarily a function of the angle of propagation.

The other approach we could have used comes from our point-source causality calculation, which also determines the time over which waves have been propagating. This approach allows us to include the influence of the acceleration of the obstacle, but not the shape of the obstacle. For the present problem, however, there is little to distinguish between the two approaches and we shall henceforth concentrate on the wavenumber-based calculation epitomized by (4.9) and (4.10).

Before turning to other issues regarding the agreement between linearized theory and the experiments, it is worth looking briefly at how the three-dimensional structure of the waves is expected to change through the depth of the finite width channel. Figure 12 plots horizontal slices through the three-dimensional wave field at a number of heights and shows the gradual two-dimensionalization of the $b_x/N^2$ fields. It is important to remember that, unlike the two-dimensional problem where the wavelength of all components is $2\pi U/N$, the wavelength in the three-dimensional problem depends on $(U/N)k/(k^2 + l^2)^{1/2}$, and so we do not expect a delta function. In addition, we note that the observed spectrum is influenced by the combined consequence of $\boldsymbol{k}$ not lying in the $x$–$z$ plane and of the patterns established by interferences from the other obstacles in our periodic array. Moreover, we note again that the $b_x$ field is sensitive only to the cross-channel average of $b'_x$ (or, equivalently, $\partial\rho'/\partial x$) and that this, in turn, is insensitive to the interference pattern. Thus, our $b_x$ fields (both experimental and theoretical) do not show the fine-grained detail of figure 12. The $b_x$ fields closest to the obstacle in figure 12 also show the Kelvin ship wave-like pattern that has been widely reported in the atmospheric literature. (Of course, in the experiments the structure is complicated further by the presence of boundary layers on the channel walls.)

It is also worth noting that the filtering imposed by the need for $m$ to be real for propagating waves means that the structure of the wave fields is relatively insensitive to the precise details of the shape of the obstacle as the high wavenumber components that give the details of the shape are evanescent and unable to propagate. Consequently, we see little qualitative difference between theory and experiment if we replace the hemisphere with a cylinder, a half-cylinder with axis aligned with the flow, or a cylinder with a vertical axis. Changing the length of the obstacle, however, can have a more direct impact on the range of wavenumbers available to propagate and the consequent shape of the lee waves. Such geometric changes also fail to capture the phase jump seen in the experiments aligned at an angle of about 53° from the vertical. We return to this last feature in § 5.

### 4.4. *One-dimensional spectra*

For a more quantitative comparison between the linearized theory and the experiments, we can consider the one-dimensional wavenumber spectra for the experiments and modified theory. Here we have computed the two-dimensional FFT $\hat{b}_x(k, m)$ of the region of $b_x(x, z)$ visible in the experiments, multiplied by the complex conjugate and expressed this in terms of the cylindrical wavenumber coordinates $(k_r, \phi)$ before shell averaging to generate the dimensionless one-dimensional spectral density as

$$P(k_r) = \frac{k_r}{2\pi R N^4} \int_{-\pi}^{\pi} \hat{b}_x \hat{b}_x^* \, \mathrm{d}\phi. \tag{4.11}$$

Figure 13 demonstrates that $P(k)$ computed for the experiment (solid curve) and linearized theory (dashed line) are relatively close, but there are clearly some discrepancies between them. In particular, the experiment appears to have its energy at slightly lower wavenumbers than the theory. Superimposed on this plot are three characteristic wavenumbers of the experimental set-up: $2\pi/H$, $2\pi/R$ and $N/U$. It is the last of these, shown as a thin vertical line, which is the most meaningful. If this were a steady, inviscid two-dimensional flow then we would expect all of the energy to lie on this line. Here, however, we have only computed the spectra from a two-dimensional projection of a three-dimensional flow in a finite domain and consequently anticipate some broadening of the observed spectral distribution. We could also see this broadening in the two-dimensional experimental spectra presented in figures 4 and 9. As we shall see later, our assumption that the dividing height $z = z_s$ is constant also contributes to the observed difference. In contrast, our somewhat arbitrary choice of $A = 1$ (in (1.5)) has little impact on the shape or positioning of the theoretical spectra, but does recover reasonably well the total energy (the integral of $P(k_r)$). We thus continue to use $A = 1$ rather than attempt to optimize the value.

### 4.5. *Angle of peak amplitude*

A key characteristic of the internal wave field that is worthy of attention is the dominant angle of the upward-propagating wave field. We noted earlier that the viscous attenuation is weakest along rays oriented at 45°. Close scrutiny of figure 11, however, shows that the strongest waves lie further from the horizontal than this angle whilst the experiments appear to have their strongest waves oriented close to 45°.

To quantify the dominant angle we could define $\Theta$, the angle between the dominant waves and horizontal, in terms of the azimuthal variation of the radially integrated power spectra. However, it proves more robust and useful to determine for each wave crest or trough the point at which $|b_x|$ is greatest and determine the best-fit line
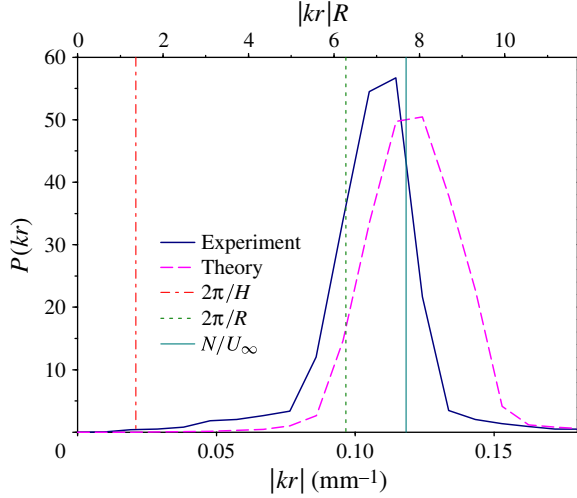
FIGURE 13. (Colour online) Comparison of one-dimensional energy spectra for experiment (solid) and linearized theory (dashed).

through all such points. This approach is similar to a criterion based on simple visual inspection. We have elected to determine the angle $\Theta(t)$ between this best-fit line and the horizontal only for the upward-propagating waves. (The reflected, downward-propagating waves yield a similar angle, but with greater scatter.)

Figure 14(*a*) shows that $\Theta(t)$ decreases slightly with time as the wave field becomes established in the $F_R = 0.18$ experiment shown in figures 7–9. While a best-fit line to the evolution of $\Theta(t)$ has been shown to highlight the decreasing trend, we anticipate the underlying temporal dependence will be an exponential decay towards an asymptotic value with a time scale related to the value of $\tau$ found in §2 for the acceleration of the flow around the channel. This modest change in angle has the opposite sense from what we might expect simply from quasisteady causality for the establishment of the accelerating flow. To illustrate this point, the bold dashed line on figure 10(*a*) plots the locus of waves emitted from the source at the angle $\theta = 45°$, corresponding to the wave component that propagates most rapidly vertically. This clearly falls below 45° (thin dotted line on the same figure), the angle that would be achieved for constant $U(t)$. However, this estimate for the dominant angle increases from $\Theta_c = 39.9°$ at $t = 120$ s to $\Theta_c = 44.3°$ at $t = 220$ s, owing to the flow asymptotically moving towards a constant speed, whereas the experimental observations of figure 14(*a*) show a modest decrease. This suggests that the difference in angle is not simply due to incomplete modelling of the quasisteady acceleration to establish the flow.

To enable a comparison across a range of different experiments, we define $\Theta_{300}$ as the value of $\Theta$ at $t = 300$ s. Repeating this calculation for a range of experiments at different topographic Froude numbers demonstrates (figure 14*b*) that this angle is a decreasing function of Froude number. This angle, however, is substantially lower than the $\Theta_{lin} = 54.0°$ that can be calculated in the same way from the linearized theory. As a comparison, two rays emanating from the top of the obstacle are plotted on figure 11. The solid line shows $\Theta_{300} = 44.0°$, our best estimate for the $F_R = 0.13$ experiment shown in figures 3 and 5 and the inset in figure 11, while the dashed line shows $\Theta_{lin} = 54.0°$. It is worth noting that this dominant angle is only weakly affected
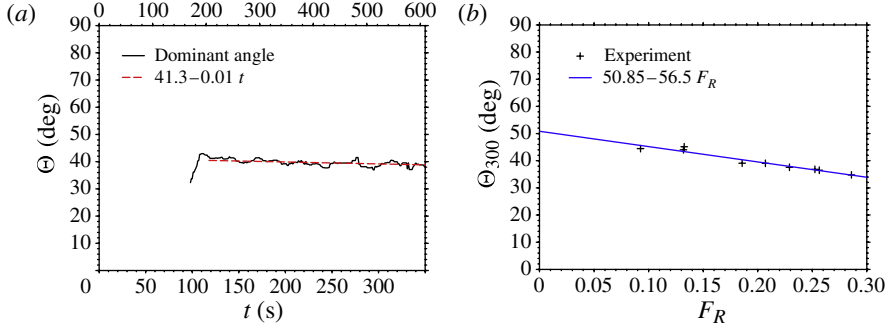
FIGURE 14. (Colour online) Dominant angle calculated from the location of the peak amplitude in the wave crests. (*a*) Evolution in time for $F_R = 0.18$. (*b*) Dominant angle as a function of topographic Froude number.
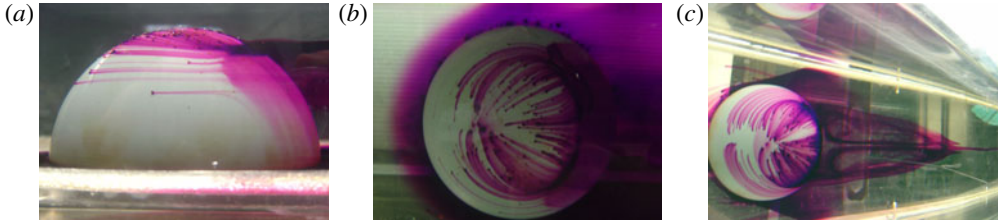


FIGURE 15. (Colour online) Dye streaks from potassium permanganate crystals lying on the surface of the obstacle showing (*a*) the separation height, (*b*) the flow on the surface of the obstacle and (*c*) the wake region below $z = z_s$ downstream of the obstacle. In each case the flow is from left to right.

by the shape assumed for the source of the waves: we were unable to find for a horizontal flow a reasonable shape (cylindrical bodies, streamlined bodies, discs, etc.) that provided a significant improvement in the agreement. We explore the cause of this discrepancy in the next section.

## 5. Non-horizontal flow

Up to this point we have assumed that the surface $z = z_s$ separating the essentially two-dimensional horizontal flow near the base of the obstacle from the wave-generating flow over the top of the obstacle is perfectly horizontal. However, while there was broad agreement between the experimental measurements and the results of linearized theory under this assumption, there are two irreconcilable differences that cannot be accounted for by experimental noise: the difference in the dominant wave angle, and the presence of a phase jump in the experimental $b_x$, visible as the wave bands discussed in § 3. We focus our attention on the first of these for the time being.

Figure 15 provides some insight into the cause of this discrepancy. Close inspection of these photographs shows that there is a clear asymmetry between the path taken by the dye streaks rising up the left-hand side of the obstacle and the path taken by the dye streaks going down on the right-hand side of the obstacle. The height of the dividing line between the horizontal flow at the base and the wave-generating flow over the cap is clearly visible in figure 15(*a*), but this also hints that it might be slightly higher on the upstream side than the downstream side. This suggestion
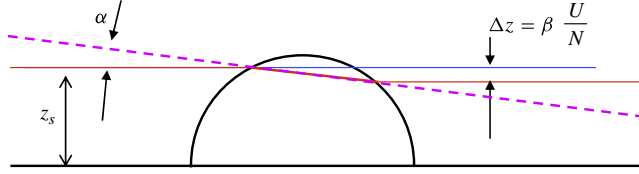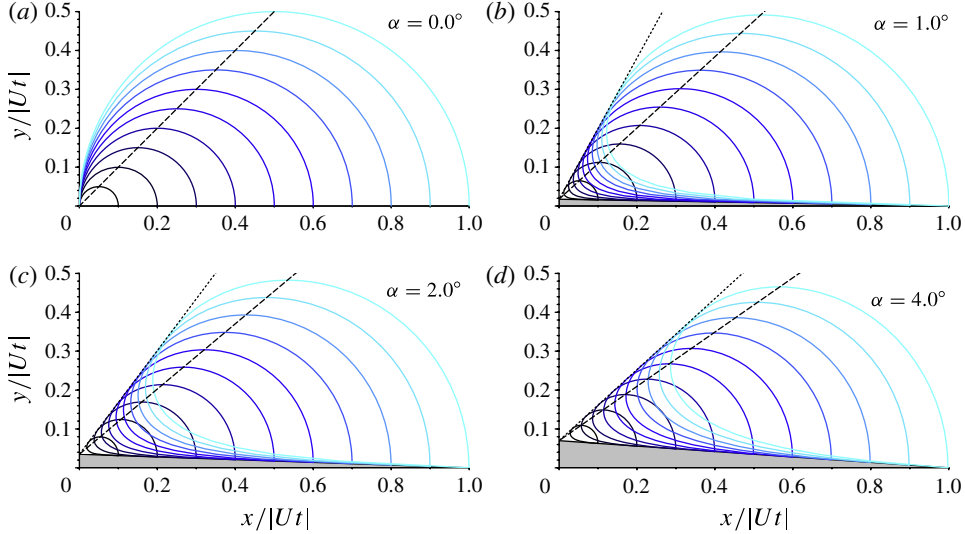
FIGURE 16. (Colour online) Sketch of tilt in the dividing streamline across the obstacle.



FIGURE 17. (Colour online) Causality curves due to a flow with a vertical component for (a) $\alpha = 0°$, (b) $\alpha = 1°$, (c) $\alpha = 2°$ and (d) $\alpha = 4°$. The dotted line shows the causality envelope for steady propagation over infinite time, while the dashed line shows the locus of the maximum vertical group velocity.

is reinforced when we consider the recirculating wake that forms below $z = z_s$ on the downstream side (figure 15c), suggesting a non-trivial form-drag and pressure difference across the obstacle. The impact of this separated wake on the velocity field was shown in figure 2(b), where the velocity near the floor of the tank was retarded significantly compared with that above the obstacle. Such a pressure difference would lead to a small tilt developing in $z = z_s$ across the obstacle, as sketched in figure 16. By equating the pressure loss with the stratification buoyancy, we anticipate that the difference in height across the obstacle will scale as $\Delta z = U/N$, and so the slope $\alpha$ will therefore scale with the topographic Froude number $F_R$. While the difference in elevation of upstream and downstream stagnation points has been discussed previously (e.g. Hunt & Snyder 1980; Hunt, Vilenski & Johnson 2006), part of its importance has remained unexplored and only becomes clear if we return to the principle of stationary phase to consider what waves can actually be sustained in such a situation.

### 5.1. *Principle of stationary phase for non-horizontal flow*

As noted in § 4.2, for a steady flow the wave field will appear stationary in the frame of reference of the obstacle as expressed by (4.3). Consider now a disturbance that is moving both horizontally and vertically relative to the fluid. Rewriting this expression
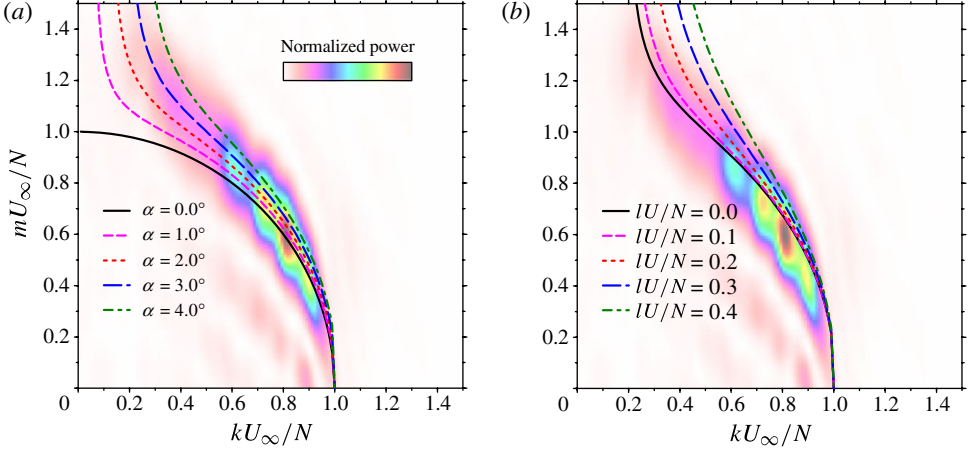
FIGURE 18. Loci of wavenumbers for propagation on a slope for (*a*) $l = 0$ and a range of different slopes $\alpha$ and (*b*) $\alpha = 3°$ and a range of different transverse wavenumbers $l$.

in terms of $N$ and the angle $\theta$ between the wavenumber vector and the horizontal gives

$$\frac{N}{\tilde{U}} = |\boldsymbol{k}|(\cos\alpha\cos\varphi - \sin\alpha\tan\theta) \tag{5.1}$$

and

$$|\boldsymbol{c}_g| = \tilde{U}(\cos\alpha\cos\varphi - \sin\alpha\tan\theta)\sin\theta. \tag{5.2}$$

Here, $\tilde{U}$ is the speed of the flow such that $U = \tilde{U}\cos\alpha$ and $W = \tilde{U}\sin\alpha$. This modified relationship controlling the wavenumbers generated by the obstacle changes the flow in a dramatic manner. Figure 17 shows how the causality shells, defined parametrically by (5.2), are changed from semicircles when $\alpha = 0$ (figure 17*a*) towards tear-drop shapes as $\alpha$ increases. Note that for $\alpha > 0$ these curves overlap, indicating the presence of interference patterns due to waves emitted at different times even for a steady flow. In addition, the envelope of the shells reaches a steady linear form, gradually extending further to the right and above the obstacle for $\alpha > 0$, whereas it only approaches a steady form asymptotically for $\alpha = 0$. The corresponding infinite time causality front rotates rapidly from the vertical as $\alpha$ increases; for small $\alpha$ the angle of the causality front is given approximately as $\Theta_f = (\pi/2) - 3((\alpha/4)^{1/3} + (\alpha/4)) + O(\alpha^{5/3})$. This leading order 1/3 power form shows just how sensitive the angle of the causality front $\Theta_f$ is to small variations in the slope. Even a very small departure from $\alpha = 0$ has a major impact on the region in which permanent waves can be found.

By considering the vertical component of $\boldsymbol{c}_g$, we can show that the waves that propagate most rapidly vertically are released at $\theta = \pi/4 - \alpha/2$, the locus of which makes an angle to the horizontal of $\Theta_z = (\pi/4) + (5/2)\alpha - 2\alpha^3 + O(\alpha^5)$ for small $\alpha$. Figure 17 shows this direction. For small $\alpha$, the direction in which waves travel most rapidly normal to the slope (not shown) falls slightly below but very close to the direction for most rapid vertical propagation. The variation with $\alpha$ of these two directions (the direction of fastest vertical propagation and the direction of fastest propagation away from the slope) will contribute to the low angle achieved in experiments.

Even though it appears that the flow close to $z = z_s$ may not be horizontal, it must return to horizontal for larger $z$ as the free surface is approached. This does not mean, however, the relevant wavenumbers return to those given by (4.7). Rather, we might expect that since the flow is nearly horizontal everywhere, then the horizontal wavenumber components $k$ and $l$ are preserved, and the frequency of the disturbance (in the frame of reference of the fluid) is preserved, thus modifying the vertical wavenumber away from that given by (4.7). Hence, (5.2) will continue to apply above and downstream of the obstacle. The relevance of (5.2) for calculating the internal waves is demonstrated clearly in figure 18 which plots solutions of this equation superimposed on the two-dimensional power spectrum of $b_x$ shown previously in figure 9(f). Figure 18(a) shows curves with $l = 0$ for a range of different slopes $\alpha$, demonstrating a clearly better match for a small departure from $\alpha = 0°$. Figure 18(b) sets $\alpha = 3°$ and shows how the transverse wavenumber $l$ changes the form of the curves. The clearly superior agreement between the experimental measurements and the theoretical prediction provides strong support for the notion that there is a small slope across the obstacle.

## 5.2. *Linearized boundary on a slope*

To complete our analysis, we now repeat our linearized boundary calculation, but using (5.2) to determine the vertical wavenumber component $m$ rather than (4.7). Again, we use causality based on a point source to determine the region where steady waves are expected, whilst the source is provided by the linearized spherical cap (now linearized relative to a slope of $\alpha = 3°$). Figure 19 shows the resulting $b_x/N^2$ fields, with the corresponding experimental image from the $F_R = 0.13$ experiment (figure 5a) shown as an inset. In both cases, rays are drawn at $\Theta_{300} = 44.0°$ (solid line), our experimental estimate of the dominant wave angle for this topographic Froude number. The dominant angle determined from our linearized boundary calculation on an $\alpha = 3°$ slope is also $44.0°$ and so indistinguishable from this. There is clearly now an extremely good correspondence between the orientations of the corresponding wave fields.

Figure 19 also reveals other experimental features not seen in the simple linearized solution on a horizontal boundary. The most noticeable of these are the phase jumps or bands in the waves emitted by the obstacle. These jumps are clearly evident in both the $b_x$ and $b_z$ fields from the experimental measurements (see figure 5a,b) but are absent from the linearized horizontal boundary model predictions (figure 11b). The orientations and relative scales of the jumps are comparable between the experiments and linearized solution, but the precise positioning relative to the object remains an imperfect match. This mismatch is probably due to the assumption that the $z = z_s$ is a simple sloping plane whereas in reality the surface is likely to have a more complex form leading to slight differences in the spectral composition of the wave field.

To emphasize again that our theoretical calculations are three-dimensional, figure 20 plots the same horizontal slices through the wave field as used for figure 12. We again see the gradual two-dimensionalization of the wave field as it propagates vertically away from the obstacle and see the reflections from the sidewalls of the channel producing an interference pattern. The marked difference, however, between figures 12 and 20 is that causality confines the waves much more laterally at low heights and displaces them further downstream at greater heights.

As anticipated, including the effect of a sloping boundary rotates the dominant wave angle towards that seen in experiments and figure 21(a) shows how $\Theta_{lin}$ changes with $\alpha$. Our choice of $\alpha = 3°$ for the comparison in figure 19 was motivated by the
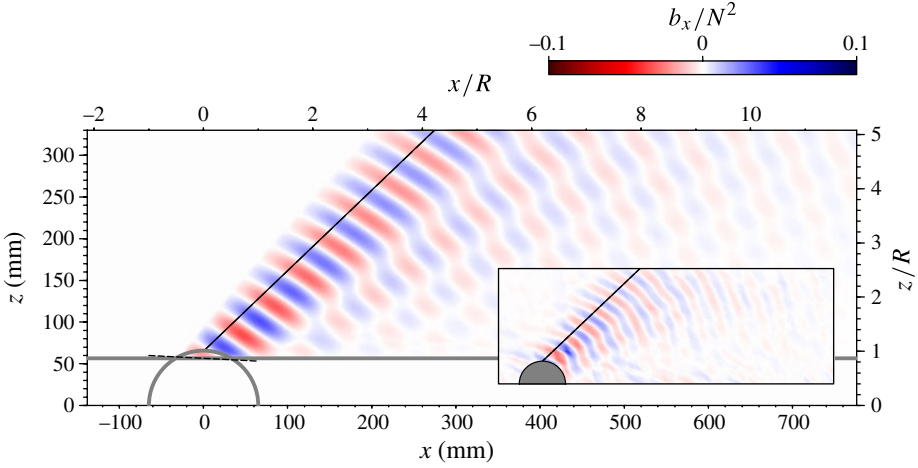
FIGURE 19. Prediction of wave field $b_x/N^2$ produced with a slope of $\alpha = 3°$ over the obstacle. The insert image (seen previously in figure 5a) shows the corresponding experimental field. Rays are shown from the top of the obstacle at angles $\Theta_{300} = \Theta_{lin} = 44.0°$.
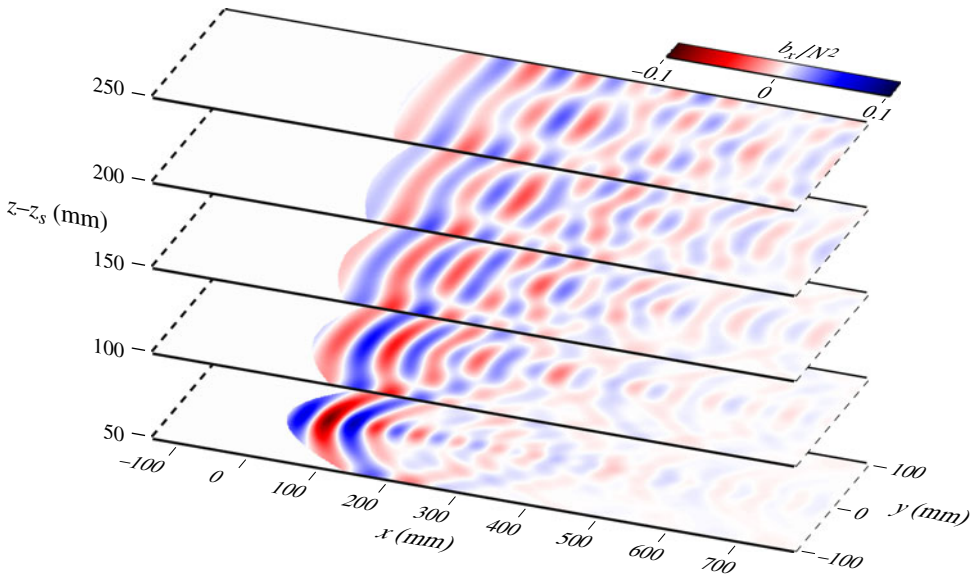


FIGURE 20. Cross-channel structure of $b'_x$ from linearized boundary calculation at 50 mm intervals above $z_s$ for a spherical cap assuming $\alpha = 3°$ tilt.

visual comparison of the wave spectra in figure 18. The resulting dominant angle, $\Theta_{lin} \approx 44.0°$, is indistinguishable from the $\Theta_{300} \approx 44.0°$ for the experimental $b_x$ field, and well within estimates of experimental uncertainty.

Figure 21(b) combines the theoretical calculation of figure 21(a) with the experimental measurements of figure 14(b) to predict the effective tilt of $z_s$ as a function of $F_R$. This relationship is approximately linear, as predicted earlier. However, we would expect it to pass through the origin, suggesting either some missing physics or, more probably, the limits imposed by experimental uncertainty.
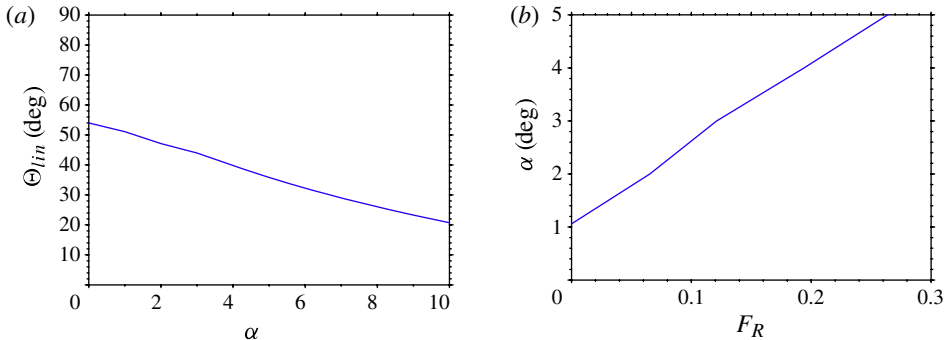
FIGURE 21. (Colour online) (*a*) Prediction from linearized theory of the change in the angle of the dominant waves with changing slope across the obstacle. (*b*) Relationship between slope $\alpha$ and topographic Froude number $F_R$ suggested by linearized theory in conjunction with experiments.

## 6. Conclusions

In this paper we have demonstrated that low topographic Froude number flow over an isolated topographic feature can be divided into two regions, as proposed by Drazin (1961) and Greenslade (1994). In particular, the obstacle can be divided into a wave-generating cap of height $\eta_0 = R - z_s = F_R R$ and a blocking base of height $z_s = (1 - F_R)R$. The height of the cap is determined by the requirement for the flow to have sufficient kinetic energy to raise fluid up and over the cap, resulting in the cap Froude number $U/N\eta_0 = 1$. Our results show that these scalings provide good energetic agreement for the lee waves produced by the cap between our experimental measurements and calculations based on linear waves and a linearized representation of the cap.

However, our results also show that it is necessary to include a small slope in the dividing surface in order to match key features of the spatial structure of the wave field. In particular, if the dividing surface is taken as horizontal then the linearized calculation fails to determine correctly the orientation of the dominant lee waves and fails to predict an observed phase jump or banding in these waves. The key additional physics incorporated through the small slope is an adjustment in the relationship between horizontal and vertical components of the wavenumber in order to preserve stationarity of the phase of the lee waves and causality. Results from experiments at a range of topographic Froude numbers shows that this small slope varies approximately linearly with the Froude number.

The structure and orientation of the wave field is extremely sensitive to small departures from horizontal flow, as witnessed by the $1/3$ power relationship between the front of the causality envelope $\Theta_f$ and the slope angle $\alpha$. In the present study, this small departure from $\alpha = 0$ is due a small slope that develops across the obstacle from the pressure difference at front and rear stagnation points. As the flow is still very nearly horizontal, the horizontal component of the wavenumber vector and the wave frequency (relative to the Lagrangian frame of the mean flow) are preserved as the waves propagate upwards and the mean flow returns to horizontal. There is an order one effect on the structure of the waves, but a much weaker effect on the energetics. This high sensitivity of the structure to the slope angle $\alpha$ is likely to be important across most geophysical flows. Although we naturally tend to think of lee waves in terms of strongly stratified flows across horizontal boundaries (e.g. the floor of the

ocean), the boundaries are seldom truly horizontal, and even if they are away from isolated topography, the flow across the topography will not be. Of course, such flows may also be influenced by planetary rotation (e.g. Riley & Lelong 2000), an effect not considered here.

We have used a simplified approach to computing the wave field, combining a steady three-dimensional linearized boundary calculation for a finite size obstacle with a causality calculation based on a quasisteady flow over a point source. Despite the finite size of the obstacle, the point source calculation has proven valuable in determining the region over which waves were found in the near field in this quasisteady accelerating flow. The computed fields were relatively insensitive to whether we modelled viscous attenuation through the steady calculation for a finite source or the quasisteady calculation for a point source. Indeed, for the sloping calculation presented in § 5.2, the differences were indistinguishable by eye and the dominant angle computed was within 1° for the two approaches.

Our experimental results are based on detailed measurements of the horizontal and vertical gradients of the cross-tank averaged buoyancy perturbation field. To help analyse this, we have introduced a new technique that allows us to divide the complete wave field into three components: (i) upward-propagating waves, issuing from the upper levels of the obstacle, (ii) downward-propagating waves resulting from reflection from the free surface and (iii) essentially horizontally propagating waves resulting from the partial blockage of the channel by the obstacle. While the upward-propagating waves have provided our main focus, we have also shown that the essentially horizontally propagating waves are the direct result of the partial blockage from the region below $z = z_s$ and are, ultimately, responsible for the slope in the dividing surface $z_s$ that develops across the obstacle.

## REFERENCES

BAINES, P. G. 1987 Upstream blocking and airflow over mountains. *Annu. Rev. Fluid Mech.* **19**, 75–97.

BAINES, P. G. 1995 *Topographic Effects in Stratified Flows*, p. 482. Cambridge University Press.

BOOKER, J. R. & BRETHERTON, F. P. 1967 The critical layer for internal gravity waves in a shear flow. *J. Fluid Mech.* **27**, 513–539.

DALZIEL, S. B., HUGHES, G. O. & SUTHERLAND, B. R. 1998 Synthetic Schlieren. In *Proceedings of the 8th International Symposium on Flow Visualization*, ed. Carlomagno & Grant, paper 062.

DALZIEL, S. B., HUGHES, G. O. & SUTHERLAND, B. R. 2000 Whole field density measurements by 'Synthetic Schlieren'. *Exp. Fluids* **28**, 322–335.

DALZIEL, S. B., CARR, M., SVEEN, K. J. & DAVIES, P. A. 2007 Simultaneous Synthetic Schlieren and PIV measurements for internal solitary waves. *Meas. Sci. Technol.* **18**, 533–547.

DRAZIN, P. G. 1961 On the steady flow of a fluid of variable density past an obstacle. *Tellus* **13**, 239–251.

GILL, A. E. 1982 *Atmosphere-Ocean Dynamics*, p. 662. Academic Press.

GREENSLADE, M. D. 1994 Strongly stratified airflow over and around mountains. In *Stably Stratified Flows: Flow and Dispersion over Topography* (ed. I.P. Castro & N.J. Rockcliff). Oxford.

GREENSLADE, M. D. 2000 Drag on a sphere moving horizontally through a stratified fluid. *J. Fluid Mech.* **418**, 339–350.

MERCIER, M. J., GARNIER, N. B. & DAUXOIS, T. 2008 Reflection and diffraction of internal waves analysed with the Hilbert transform. *Phys. Fluids* **20**, 086601.

HAZEWINKEL, J., GRISOUARD, N. & DALZIEL, S. B. 2010 Comparison of laboratory and numerically observed scalar fields of an internal wave attractor. *Eur. J. Mech. (B/Fluids)* **30**, 51–56.

HUNT, J. C. R & SNYDER, W. H. 1980 Experiments on stably and neutrally stratified flow over a model three-dimensional hill. *J. Fluid Mech.* **9**, 671–704.

HUNT, J. C. R., VILENSKI, G. G. & JOHNSON, E. R. 2006 Stratified separated flow around a mountain with an inversion layer below the mountain top. *J. Fluid Mech.* **556**, 105–119.

HUPPERT, H. E. & MILES, J. W. 1969 Lee waves in a stratified flow. Part 3. Semi-elliptical obstacle. *J. Fluid Mech.* **35**, 481–496.

LIGHTHILL, M. J. 1978 *Waves in Fluids*, p. 504. Cambridge University Press.

LONG, R. R. 1955 Some aspects of the flow of stratified fluids III. Continuous density gradients. *Tellus* **7**, 341–357.

MILES, J. W. 1961 On the stability of heterogeneous shear flows. *J. Fluid Mech.* **10**, 496–508.

MILES, J. W. & HUPPERT, H. E. 1968 Lee waves in a stratified flow. Part 2. Semi-circular obstacles. *J. Fluid Mech.* **33**, 803–814.

ODELL, G. M. & KOVASZNAY, L. S. G. 1971 A new type of water channel with density stratification. *J. Fluid Mech.* **50**, 535–543.

RILEY, J. J. & LELONG, M.-P. 2000 Fluid motions in the presence of strong stable stratification. *Annu. Rev. Fluid Mech.* **32**, 613–657.

SCASE, M. M. & DALZIEL, S. B. 2006 Internal wave fields generated by a translating body in a stratified fluid: an experimental comparison. *J. Fluid Mech.* **564**, 305–331.

SCORER, R. S. 1949 Theory of waves in the lee of mountains. *Q. J. R. Meteorol. Soc.* **75**, 41–56.

SUTHERLAND, B. R., DALZIEL, S. B., HUGHES, G. O. & LINDEN, P. F. 1999 Visualisation and measurement of internal waves by 'Synthetic Schlieren'. Part 1. Vertically oscillating cylinder. *J. Fluid Mech.* **390**, 93–126.

TURNER, J. S. 1973 *Buoyancy Effects in Fluids*, p. 367. Cambridge University Press.

VOISIN, B. 1994 Internal wave generation in uniformly stratified fluids. Part 2. Moving point sources. *J. Fluid Mech.* **261**, 333–374.

VOISIN, B. 2007 Lee waves from a sphere in a stratified flow. *J. Fluid Mech.* **574**, 273–315.

VOSPER, S. B., CASTRO, I. P., SNYDER, W. H. & MOBBS, S. D. 1999 Experimental studies of strongly stratified flow past three-dimensional orography. *J. Fluid Mech.* **390**, 223–249.

WURTELE, M. G., SHARMAN, R. D. & DATTA, A. 1996 Atmospheric lee waves. *Annu. Rev. Fluid Mech.* **28**, 429–476.